UNIVERSITY OF AMSTERDAM

UvA-DARE (Digital Academic Repository)

Be-star discs and non-radial pulsations in rotating stars

Telting, J.H.

Publication date
1996

[Link to publication](#)

Citation for published version (APA):
Telting, J. H. (1996). *Be-star discs and non-radial pulsations in rotating stars*.

Be-star discs

Chapter 3

Long-term periodic variability in UV absorption lines of the Be star γ Cas: on the relation with V/R variations in the Hβ line [*]

John H. Telting and Lex Kaper

Astronomical Institute Anton Pannekoek, University of Amsterdam, and Center for High Energy Astrophysics, Kruislaan 403, 1098 SJ Amsterdam, Netherlands

Abstract. We present a quantitative study of the variability in ultraviolet resonance lines of N v, Si iv and C iv of the Be star γ Cas. For this purpose we used IUE spectra obtained over a period of eleven years. Variability occurs in the form of discrete absorption components (DACs), which are formed in the fast-outflowing radiatively driven part of the stellar wind. We constructed a template spectrum from spectra containing no or minor extra absorption due to DACs and modelled the isolated DACs in the obtained quotient spectra. Besides the frequently observed narrow components (v_t typically ≤ 250 km/s) at high velocity, we found several broad components occurring at low and intermediate wind velocities.

We confirm the finding of Doazan et al. (1987) who reported that the number of observed DACs is associated with the cyclic V/R variability of the Balmer-emission lines. We show that when V/R<1 the central optical depth of DACs is significantly lower than when V/R>1. In our interpretation this is due to a correlation between the column density associated with the DACs and the phase of the V/R cycle.

We find that the Hβ observations of Doazan et al. are consistent with a model in which the cyclic V/R variability is due to a global, one-armed oscillation moving through an equatorial disc. We suggest that the higher column density of DACs in phases of V/R>1 is the result of the higher density in the region of their origin, namely close to or in the part of the equatorial disc which is rotating towards the observer.

1. Introduction

By definition a B star is classified as Be if the Hα line has once been observed in emission and the star is not a supergiant. Be stars display a wide range of specific properties. Among those are rapid rotation and extreme spectral variability on time scales ranging from hours to decades. Extended reviews describing the properties of Be stars are presented by e.g. Doazan (1982) and Slettebak (1988).

Various observations of Be stars over a broad range of the spectrum indicate that Be stars have a non-spherical envelope. The energy distribution shows an excess due to free-free radiation from the near IR (Gehrz et al. 1974), through the far IR (Coté and Waters 1987), to the radio domain (Taylor et al. 1987). Coté and Waters found that Be stars with a large IR excess at 12μ show polarization in the visual, and suggested that the IR excess is caused by a non-spherical density distribution. The Balmer emission lines have widths of a few hundred km/s and are often double-peaked, which can be understood if the line-forming region is rotating (see e.g. Sobolev 1960, Huang 1972, Marlborough 1969). These emission lines are pri-

marily formed by recombination in circumstellar matter. Dachs et al. (1986) conclude that the shape of measured Hα profiles is consistent with the expected shape of profiles originating in a flat differentially rotating disc-shaped envelope. Further observational support for the presence of an equatorial disc in Be-star envelopes results from X-ray observations of Be/X-ray binaries (e.g. Van den Heuvel and Rappaport 1987). To explain the X-ray luminosity by accretion of wind material on a compact object, a dense low-velocity outflow in the equatorial plane is needed (Waters et al. 1988, Waters 1989). Furthermore, Dougherty and Taylor (1992) have resolved the circumstellar envelope of the Be star ψ Per at 15 GHz, and find that this envelope is highly non-spherical. All the above mentioned observations are consistent with the presence of a slowly expanding, relatively high-density, disc-like wind around Be stars.

UV observations show that Be stars also have winds with terminal velocities in the order of 1000 km/s, which are observed in resonance lines of N v, Si iv and C iv. The derived mass-loss rates of $10^{-9} - 10^{-11}$ M$_\odot$/yr and the dependence of these rates on stellar luminosity (Snow 1982) suggest that these stellar winds are radiatively driven, like the winds of more luminous O and OB supergiant stars, although Abbott (1982) argues that radiation-driven winds of cooler B-type stars can not be self-initiating. The mass-loss rates derived from the IR

---

excess, however, are a factor of 10^2 to 10^4 times larger than those derived from the UV (Waters et al. 1987).

To combine these two types of stellar winds a two-component model describing the Be-star envelope was proposed (see e.g. Telting et al. 1993 for the case of γ Cas): a dense equatorial (differentially rotating) disc in which the Balmer emission lines and the IR excess are formed, and a rapidly expanding radiation-driven wind streaming from higher latitudes of the star, which forms the UV resonance lines. Recent work of Bjorkman and Cassinelli (1993) gives a physical basis for the presence of an equatorial disc in rapidly rotating B-type stars. If the rotation speed exceeds a critical value, the supersonic wind that leaves the stellar surface at high latitude travels along trajectories that cross the equatorial plane. A dense equatorial disc is formed due to ram pressure confinement of the stellar wind.

Variability occurs in both types of the Be stellar wind. Long-term variability (time scales of 2–15 years) in the ratio of the intensity of the violet and red peak of the Balmer emission lines (V/R variation) is commonly observed in the spectra of Be stars (see e.g. Dachs 1987). Telting et al. (1993) discussed, based on observations of γ Cas, models that may explain this V/R behaviour. They concluded that the model which is most consistent with both V/R and IR continuum observations consists of a star surrounded by a rotating non-axisymmetric, disc-like wind, which is not face-on. Physical models for the cause of asymmetry in disc-like structures are given by Okazaki (1991) and Papaloizou et al. (1992), who discuss global one-armed oscillations. Papaloizou et al. found that due to the gravitational potential of an oblate (i.e. rapidly rotating) star, oscillations in the disc on time scales of V/R variations can exist.

Many Be stars show variable discrete absorption components (DACs) in UV resonance lines (Henrichs 1984, Grady et al. 1987, Prinja 1989). A remarkable fact is that all B-type stars with $M_V \geq -7$ mag that show DACs are Be stars. DACs appear in UV spectra of more than 80% of all O-type stars (Howarth and Prinja 1989). The origin of DACs is not known.

Doazan et al. (1989) found observational evidence for a correlation between the long-term cyclic V/R variability and changes of the equivalent width of UV resonance lines of the Be star 59 Cyg. Doazan et al. (1987) report evidence for a correlation between the Hβ V/R variability and the occurrence/presence of DACs in UV lines of γ Cas. These observations indicate that the equatorial and polar wind regions are somehow linked.

γ Cassiopeiae (HR264, HD5394) was the first emission line star that was discovered (Secchi 1867) and is one of the best studied Be stars. Its visual magnitude ($m_V \approx 2.25$) makes γ Cas the brightest Be star of the northern hemisphere. Its spectral type is B0.5 IVe (Lesh 1968) and $v \sin i = 230$ km/s (Slettebak 1982).

Doazan et al. (1983) and Goraya and Tur (1988) give detailed descriptions of long-term variations in the optical spectrum of γ Cas. This century γ Cas underwent two phases of Balmer emission. The first one ended in a B phase after spec-

tacular light and spectral variations, including V/R variations, and two B-shell episodes. Presently γ Cas is in the second Be phase of this century, which started around 1946. Since then the visual brightness is gradually increasing. V/R variation of the Balmer lines began around 1970 and has a cyclic behaviour with an increasing period of about 5 ± 2 years. The Balmer emission lines showed no V/R variations between 1946 and 1970.

The presence of DACs in spectra of γ Cas was first discovered by Hammerschlag-Hensberge (1979), who found blue-shifted absorption enhancements in the resonance lines of N V, Si IV, and C IV. Henrichs et al. (1983) studied the properties of DACs in ultraviolet spectra of γ Cas obtained from 1978 to 1980. They found that DACs were present in 18 out of the 28 spectra. Doazan et al. (1987) reported that "the occurrence of high-velocity DACs in UV resonance lines exhibits a long-term variability pattern, which is associated with the cyclic V/R variations of the Balmer emission lines. DACs are frequently observed when V/R>1, while they are absent or rarely present when V/R<1".

The objective of this study is to quantify the correlation between DAC variability in UV resonance lines and the observed V/R variability of the Hβ line of γ Cas. We used 133 archival IUE spectra of γ Cas , which were obtained from 1978 to 1989. We use the method of Henrichs et al. (1983) to derive central velocities, central optical depths, widths, and column densities of DACs. In the next section we describe the reduction of the high-resolution IUE images of γ Cas. In section 3 we discuss the analysis of these spectra. We describe our DAC fitting method in section 4 and summarize the fit results in section 5. In section 6 the results are compared with the V/R variability of the Hβ line. In section 7 we discuss the implications of the correlative behaviour of DAC and V/R variability and discuss a model which might explain the observations. In the last section our conclusions are summarized.

2. Observations and reduction

Table 1 presents a listing of the collected high-resolution ultraviolet spectra of γ Cas. These IUE spectra were selected to give a complete coverage with sufficient time resolution (see e.g. Fig. 8) of the occurrence and persistence of discrete absorption components in resonance doublet lines of N V, Si IV and C IV (see Table 2). The selected spectra were taken in the years 1978 through 1989 with the Short-Wavelength Prime (SWP) camera (1150–1950 Å), mostly in the large aperture (LAP) mode. The spectra have a spectral resolution of about 0.05 Å. A description of the instrument is given by Boggess et al. (1978a,b).

Raw data from the IUE satellite were processed at the ground stations GSFC and VILSPA with the IUESIPS#1 and IUESIPS#2 data reduction packages. We reduced the resulting GPHOT and PHOT images with the IUEDR software package (Giddings 1983a,b). The IUEDR program provides spectrum extraction, wavelength calibration, improved inter-order background subtraction and echelle ripple calibration, which is all briefly discussed in the following.

Table 1. List of selected IUE spectra of γ Cas. The first column gives the SWP image number of the spectra. The column marked `A` specifies which aperture was used during the observation (Small or Large). The column marked `C` lists the factor which was used to scale the spectrum to the intensity of the average spectrum. Images marked with an asterisk were used to construct a template spectrum (see Sect. 3)

SWP image	A	date	J.D. −2440000	C	SWP image	A	date	J.D. −2440000	C	SWP image	A	date	J.D. −2440000	C
1449	S	'78 May 01	3630	0.742	16159	S	'82 Jan 28	4998	0.665	20988	L	'83 Sep 09	5587	1.102
2294	S	Aug 14	3735	0.588	16161	S	Jan 28	4998	0.667	21581	L	Nov 19	5658	1.071
2385	S	Aug 24	3745	0.708	16163	S	Jan 28	4998	0.742	*21771	L	Dec 14	5683	1.053
2470	S	Sep 04	3756	0.540	16167	S	Jan 28	4998	0.733	22760	L	'84 Apr 16	5807	1.063
2681	S	Sep 18	3770	0.714	16284	S	Feb 08	5009	0.670	24001	L	Sep 19	5963	1.086
4640	S	'79 Mar 15	3948	0.727	16518	L	Mar 12	5041	1.121	25238	L	'85 Feb 14	6111	1.047
5928	S	Jul 24	4079	0.593	16528	L	Mar 14	5043	1.114	26338	L	Jul 02	6249	1.053
5929	S	Jul 24	4079	0.659	16694	L	Apr 05	5065	0.542	*26822	L	Oct 01	6340	1.066
6268	L	Aug 23	4109	1.080	17093	L	Jun 01	5122	1.060	27268	L	Dec 14	6414	1.049
6786	L	Oct 07	4154	0.709	17588	S	Aug 04	5184	0.528	27390	L	Dec 26	6426	1.033
6902	L	Oct 18	4165	1.105	17859	L	Sep 06	5219	1.093	27391	L	Dec 26	6426	1.037
6903	L	Oct 18	4165	1.113	*17878	L	Sep 08	5221	1.083	27607	L	'86 Jan 26	6457	1.048
6904	L	Oct 18	4165	1.123	17881	L	Sep 08	5221	1.090	27669	L	Feb 06	6468	1.043
7890	S	'80 Feb 08	4278	0.655	17900	L	Sep 09	5222	1.081	28555	L	Jun 27	6609	1.038
8554	L	Mar 25	4324	1.118	17916	L	Sep 11	5224	1.145	28601	L	Jul 03	6615	1.050
8666	L	Apr 05	4335	1.105	17921	L	Sep 11	5224	1.157	28724	L	Jul 20	6632	1.073
9129	L	May 26	4386	1.113	17935	L	Sep 12	5225	1.085	28841	L	Aug 05	6648	1.075
9130	L	May 26	4386	1.060	17951	L	Sep 14	5227	1.159	29269	L	Sep 21	6695	1.063
9897	S	Aug 25	4477	0.701	17967	L	Sep 15	5228	1.106	29343	L	Oct 01	6705	1.043
10863	S	Dec 22	4596	0.697	17974	L	Sep 16	5229	1.143	29379	L	Oct 05	6709	1.045
14274	L	'81 Jun 18	4774	1.049	17978	L	Sep 16	5229	1.150	29416	L	Oct 10	6714	1.017
14430	L	Jul 09	4795	1.074	*17979	L	Sep 16	5229	1.153	29645	L	Nov 10	6745	1.046
14760	L	Aug 14	4831	1.058	18011	L	Sep 18	5231	1.108	29666	L	Nov 13	6748	1.037
14968	L	Sep 12	4860	1.069	*18034	L	Sep 20	5233	1.153	29848	L	Dec 10	6775	0.991
14988	L	Sep 14	4862	1.083	18051	L	Sep 21	5234	1.098	29853	L	Dec 11	6776	1.006
14989	L	Sep 14	4862	1.095	18072	L	Sep 23	5236	1.161	30262	L	'87 Feb 06	6833	0.995
15015	L	Sep 16	4864	1.129	18097	L	Sep 24	5237	1.076	30445	L	Mar 06	6862	1.048
*15034	L	Sep 18	4866	1.080	18127	L	Sep 27	5240	1.168	31350	L	Jul 17	6994	1.014
15043	L	Sep 19	4867	1.091	*18136	L	Sep 27	5240	1.100	31513	L	Aug 08	7016	1.073
15063	L	Sep 20	4868	1.106	18164	L	Sep 30	5243	1.062	31903	L	Sep 22	7061	1.029
*15064	L	Sep 20	4868	1.108	*18182	L	Oct 02	5245	1.116	32676	L	'88 Jan 06	7167	1.031
15119	L	Sep 28	4876	1.067	18188	L	Oct 02	5245	1.073	32923	L	Feb 04	7196	1.034
15139	L	Sep 30	4878	1.069	*18206	L	Oct 05	5248	1.116	35079	L	Dec 20	7516	0.998
15206	L	Oct 08	4886	1.062	*18231	L	Oct 07	5250	1.156	35582	L	'89 Feb 19	7577	0.998
15227	L	Oct 10	4888	1.055	18249	L	Oct 11	5254	1.122	*35583	L	Feb 19	7577	1.006
15254	L	Oct 13	4891	1.069	18258	L	Oct 11	5254	1.094	35584	L	Feb 19	7577	1.012
*15278	L	Oct 16	4894	1.060	*18277	L	Oct 14	5257	1.148	35585	L	Feb 19	7577	1.017
15299	L	Oct 20	4898	1.084	*18278	L	Oct 14	5257	1.155	35586	L	Feb 19	7577	1.014
15466	L	Nov 09	4918	1.050	18319	L	Oct 18	5261	1.168	35587	L	Feb 19	7577	1.023
15702	L	Dec 10	4949	1.075	*18345	L	Oct 21	5264	1.096	35588	L	Feb 19	7577	1.027
16127	S	'82 Jan 27	4997	0.524	19097	L	'83 Jan 27	5362	1.084	35589	L	Feb 19	7577	1.025
*16131	S	Jan 27	4997	0.637	19656	L	Apr 06	5431	1.077	35590	L	Feb 19	7577	1.028
16133	S	Jan 27	4997	0.563	20312	L	Jun 25	5511	1.098	*35591	L	'89 Feb 19	7577	1.011
16135	S	Jan 27	4997	0.617	*20642	L	Aug 08	5555	1.070					
16157	S	'82 Jan 28	4998	0.662	*20673	L	'83 Aug 13	5560	1.143					

We extracted echelle orders #66 to #125, corresponding to the wavelength range 1150–1950 Å. Small and large aperture GPHOT and PHOT images were sampled at a single spacial grid (spacing of $\sqrt{2}$ pixels), which enabled us to apply the same data reduction simulation in our fit routines (see Sect. 4.1) for all types (PHOT and GPHOT) of spectra.

Wavelength calibration was performed by matching the wavelengths of interstellar lines of FeII ($\lambda = 1608.456$ Å), SiIII ($\lambda = 1304.372$ Å) and SII ($\lambda = 1253.812$ Å and $\lambda = 1259.520$ Å) to their laboratory wavelengths. We checked the positioning of the wavelength scale using the interstellar lines of CII ($\lambda = 1335.70$ Å) and SiIII ($\lambda = 1526.71$ Å). We find the error in the wavelength scale to be less than 5 km/s. We did not correct for the radial space velocity of the star which is about 4 km/s (Ferlet et al. 1980).

The background illumination was estimated by inter-order count rates. In spectral regions where the echelle orders are very close, the signal from the object itself can spread into the inter-order regions of the image, and, consequently, the background intensities in these spectral regions will be over-estimated. Therefore, a semi-empirical background correction method which is based on the work of Bianchi and Bohlin (1984) is applied. This method corrects the background subtraction for wavelengths shorter than 1400 Å. We adopted a halation correction factor of HALC = 0.15 for all spectra.

Echelle ripple correction was done by an algorithm developed by Barker (1984). This algorithm scales the flux values of adjacent orders such that the orders overlap properly.

The spectra were mapped on a uniform wavelength grid with a spacing of 0.1 Å. For every wavelength point the intensity is given in fluxnumbers per second. We could not convert these intensities to normal flux units because no proper absolute flux calibration for high-dispersion IUE spectra is available.
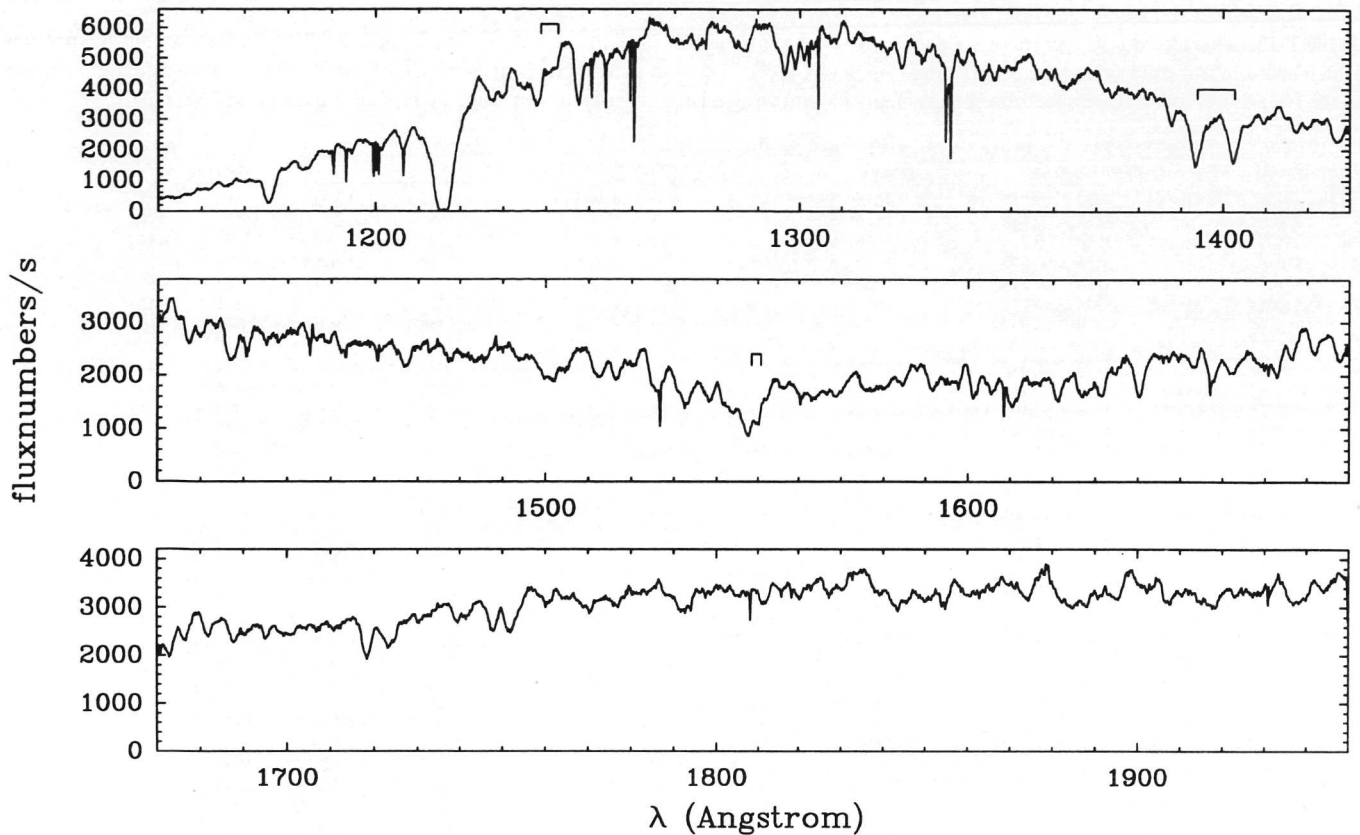
Fig. 1. Average of all 133 spectra of γ Cas listed in Table 1, covering the whole wavelength range of the SWP camera (1150–1950 Å). Rest wavelengths of the doublets of interest are indicated

The spectra were smoothed over the reseau marks by linear interpolation between the average flux values of three wavelength points on either side of a reseau mark.

To be able to compare the DAC behaviour with the long-term V/R variations as observed in the Balmer emission lines, we collected Hβ V/R data from the literature. We use Hβ data of γ Cas which were obtained in 1969–1976 by Cowley et al. (1976), and in 1976–1986 by Doazan et al. (1987). These data are plotted in e.g. Fig. 11b. V/R measurements of other Balmer lines do not have a time coverage as complete as that of the Hβ line.

3. Analysis of the UV spectra of γ Cas

Flux scaling. In Fig. 1 we present the average of the 133 spectra of γ Cas. It appeared that the continuum levels of individual small aperture (SAP) spectra could deviate up to 48% from the continuum level of the average spectrum, which might be the result of incorrect centering of the stellar image in the aperture. To facilitate the comparison of the spectra we scaled each spectrum such that the integrated flux in five well-chosen wavelength regions is the same as in the average spectrum. Scaling factors were derived for wavelength domains in which we do

not expect to find variability: 1155–1210 Å (C_1), 1265–1300 Å (C_2), 1430–1500 Å (C_3), 1580–1680 Å (C_4) and 1760–1810 Å (C_5). We divided the integrated flux of a domain by the integrated flux of the same domain of the average spectrum. For each spectrum we averaged the five scaling factors weighted by the number of wavelength points of each region. We used the resulting average to scale each complete SWP spectrum. The average scaling factors are listed in Table 1.

Template spectrum for wavelength regions with DACs. In order to isolate the discrete absorption components occurring in the resonance doublets of N V, Si IV and C IV , we constructed a template spectrum from spectra with presumably no DACs present: we averaged the 20 scaled spectra with the highest integrated flux in the spectral regions where DACs occur, 1230–1247 Å, 1385–1406 Å and 1538–1553 Å. The spectra thus selected are marked by a star in Table 1; 19 LAP spectra each with 8 seconds exposure time and one SAP spectrum with 12 seconds exposure time. Over the full SWP wavelength range the fluxes of these scaled spectra overlap within the noise (S/N $\sim$ 25). Parts of the template spectrum and image SWP29343 are plotted in Fig. 2, which shows that these two spectra are practically identical except in those wavelength regions where DACs occur.
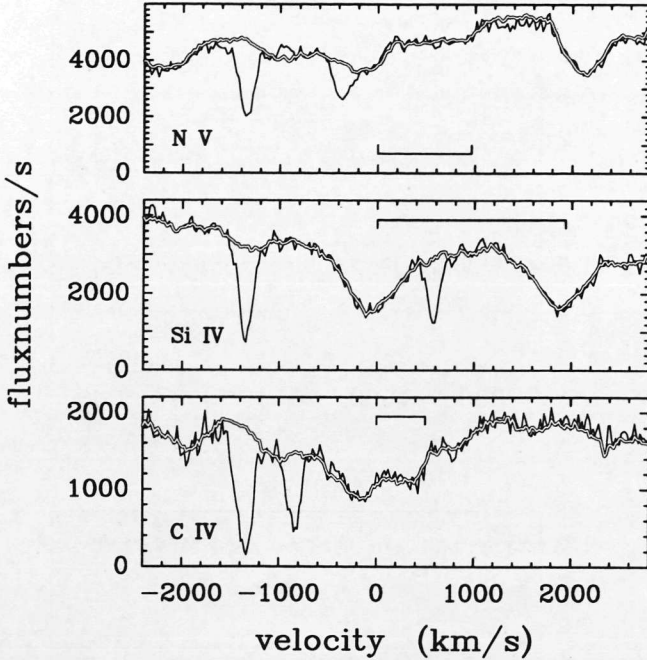
Fig. 3. Relative standard deviation of the flux values per wavelength point, $\sigma_{F_\lambda}/<F_\lambda>$, of the 20 template spectra (see Table 1) as a function of the mean flux at that wavelength, $<F_\lambda>$. Solitary points are due to reseau marks. The hollow line depicts the average in bins of 200 FN/s

Fig. 2. Template spectrum (hollow curve) and image SWP29343 (solid curve) on a velocity scale around the N V, Si IV and C IV resonance doublets. The velocity scale is relative to the rest wavelength of the short-wavelength doublet line. Rest wavelengths of the doublet lines are indicated

The shapes of the persistent P Cygni profiles in our template are very similar to the shapes seen by Henrichs et al. (1983), who used spectra observed in 1980. We see maximum absorption at approximately -200 km/s, -100 km/s and -150 km/s for the N V, Si IV and C IV principal doublet lines respectively. The FWHM of the principal Si IV doublet line is at least 600 km/s, which is larger than twice the measured projected rotation velocity ($v\sin i \sim 230$ km/s). The asymmetric shape of the doublet profiles and the large FWHM of the doublet lines clearly indicate that these lines are formed in the rapidly outflowing wind of the star.

Error determination for detected flux values. The 20 scaled spectra from which the template is built are relatively DAC free, and can therefore be used to estimate the noise at a wavelength point as a function of flux. We defined the variance of the flux values per wavelength point as

$$\sigma_{F_\lambda}^2 = \frac{\left(\sum F_\lambda^2\right) - \left(\sum F_\lambda\right)^2/N_{spec}}{\left(N_{spec} - 1\right)} \tag{1}$$

where $N_{spec} = 20$ is the number of spectra considered and F_λ is the scaled flux of each of the 20 spectra at wavelength λ, given in fluxnumbers per second (FN/s). Figure 3 displays the relative standard deviation of the flux at a given wavelength as a function of the mean flux value, $<F_\lambda>$, at that wavelength. One can see that towards low flux values the relative deviation increases

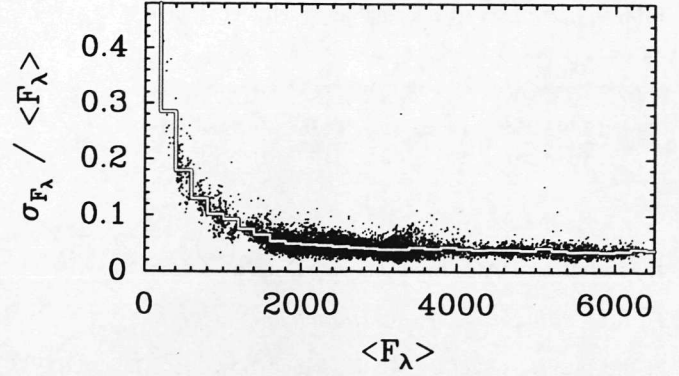and that for flux levels higher than $F_\lambda \sim 1500$ FN/s the relative error is approximately 0.04. We binned the determined relationship in bins of 200 FN/s. We omitted wavelength points longward of 1925 Å, because reseau marks in this wavelength region tend to drift and also fluctuate in size (i.e. they cover varying wavelength ranges), thus giving rise to incorrect error estimates. Over 7500 wavelength points were used to derive the relationship between σ_{F_λ} and $<F_\lambda>$, which we used to fit models to the spectral data (Sect. 4.2).

Normalization. In order to be able to fit our model of discrete absorption components to the ultraviolet spectra of γ Cas we divided each scaled spectrum by the template spectrum. We defined the normalized flux as

$$I_\lambda = F_\lambda/F_\lambda^{template} \tag{2}$$

where $F_\lambda^{template}$ is the flux of the template spectrum at wavelength λ. We estimated the error of the normalized flux using the previously derived relationship for σ_{F_λ} and the measured flux, and the following relation for the relative standard deviation of the normalized flux values, σ_{I_λ}:

$$\left(\frac{\sigma_{I_\lambda}}{I_\lambda}\right)^2 = \left(\frac{\sigma_{F_\lambda}}{F_\lambda}\right)^2 + \left(\frac{\sigma_{F_\lambda^{template}}}{F_\lambda^{template}}\right)^2 /N_{spec}. \tag{3}$$

Two examples of normalized (i.e. quotient) UV spectra of γ Cas are displayed in Fig. 4. This figure shows the spectral regions of the N V, Si IV and C IV doublets, for a spectrum with and a spectrum without DACs. The regions with higher noise correspond to lower flux values in the original spectrum. The average flux is highest in the N V region and lowest in the C IV region (see Fig. 2). This gives rise to the different overall noise levels seen in the different normalized spectral regions.

We have used the quotient spectra to derive model parameters for DACs, if present. We emphasize that all derived quantities we present are given with respect to the template, i.e. they correspond to properties of the isolated DACs themselves.

Table 2. Laboratory wavelengths and oscillator strengths

	λ_1 in Å	λ_2 in Å	f_1	f_2
N v	1238.808	1242.796	0.156	0.0778
Si iv	1393.755	1402.770	0.536	0.266
C iv	1548.188	1550.762	0.190	0.0950

4. Modelling DACs in resonance lines of γ Cas

4.1. Modelling discrete absorption components

In the previous section we described how we converted 133 high-resolution IUE spectra of γ Cas to quotient spectra with respect to a template. By dividing through the template we assume that the material forming the DACs does not influence the shape of the persistent P Cygni profile that is formed by the steady high-velocity wind. To relate the observed absorption enhancements in the quotient spectra to column densities, we apply the theory of resonance-line radiation-transfer in expanding atmospheres as described by Caroff et al. (1972) and Lucy (1984), to the case of outflowing local density enhancements of the stellar wind. These authors consider the formation of a resonance line by pure scattering in a rapidly and differentially expanding atmosphere. Photons of the central source are scattered out of the line of sight, resulting in blue-shifted absorption. Under the conditions as described in these papers the optical depth is proportional to the reciprocal velocity gradient of the gas:

$$\tau = \frac{\pi e^2}{m_e c} n_i f \frac{c}{\nu_0} \left(\frac{dv}{dr} \right)^{-1} \tag{4}$$

where c is the speed of light, ν_0 is the laboratory frequency of the resonance line, e is the elementary charge in E.S.U., m_e the electron rest mass and f the oscillator strength of the transition of interest.

If we assume that DACs are formed in dense outflowing plane-parallel slabs in the line of sight in which the plasma has a Maxwellian velocity distribution, we can apply the formalism given by Henrichs et al. (1983) to model single-line absorption profiles in normalized spectra. Ignoring the intrinsic flux contribution of the material in the slabs they adopt

$$I(v) = \exp(-\tau_c \phi(v)) \tag{5}$$

with the Gaussian profile function

$$\phi(v) = \exp \left\{ - \left(\frac{v - v_c}{v_t} \right)^2 \right\}, \tag{6}$$

where v is the velocity with respect to the stellar rest frame, τ_c is the optical depth at the centre of the line, v_c is the Doppler displacement of the centre of the line, and where v_t is the broadening parameter in units of velocity. It is assumed that for a doublet the velocity displacement and the broadening parameter are the same for both doublet lines. With velocity scaled to the
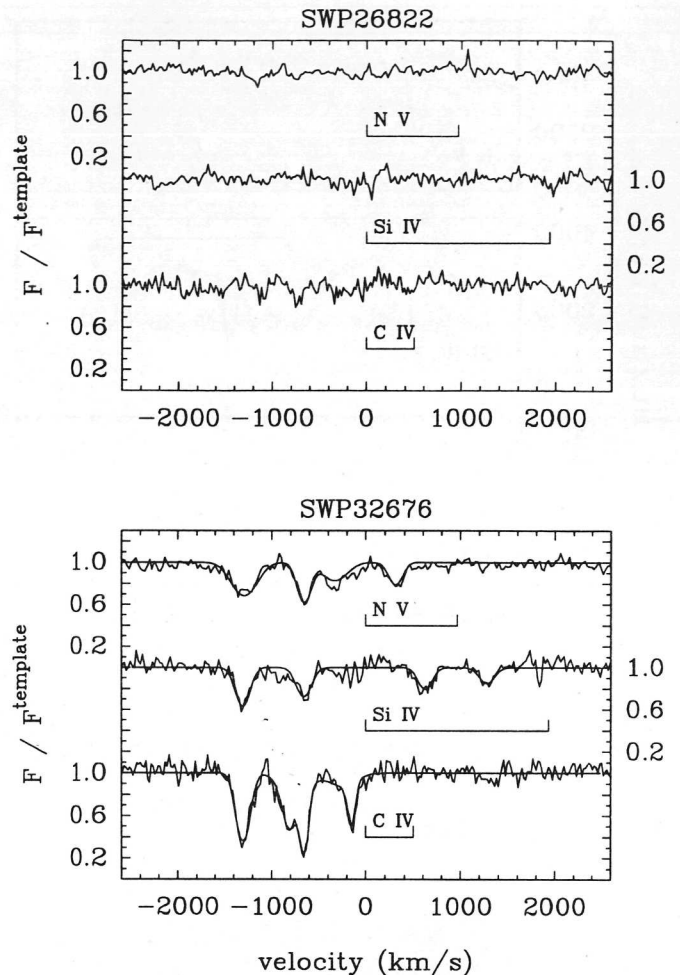
Fig. 4. Residual spectra of two high-resolution SWP images of γ Cas around the N v, Si iv and the C iv resonance doublets. Rest wavelengths of the doublet lines are indicated. Velocities are relative to the rest wavelength of the principal doublet lines. **Top)** Normalized spectrum of image SWP26822. The spectrum seems free of DACs. This spectrum is one of the spectra selected to create the template. **Bottom)** Normalized spectrum of image SWP32676 with fitted DAC models. This spectrum clearly shows multiple DACs

rest wavelength of the principal line of the doublet, the shifted central velocities of the doublet lines are related as

$$v_2 = \frac{\lambda_2}{\lambda_1} v_1 + \frac{\lambda_2 - \lambda_1}{\lambda_1} c . \tag{7}$$

Indices 1 and 2 refer to the principal and secondary doublet line respectively. We define the doublet separation $v_{\rm split}$ (in km/s) as

$$v_{\rm split} = v_2 - v_1 = (v_1 + c) \left(\frac{\lambda_2 - \lambda_1}{\lambda_1} \right) . \tag{8}$$

Following Henrichs et al. (1983) the column density of an absorption component, N_{col}, can be expressed, using Eqs. (4) and (6), as

$$N_{col} = \frac{m_e c}{\pi e^2} \frac{\sqrt{\pi}}{f \lambda_0} \frac{\tau_c v_t}{(1 + v_c/c)}, \qquad (9)$$

which gives the column density for either of the two components of the doublet. In this equation λ_0 is the laboratory wavelength of the considered line. Since the derived column densities of both doublet components are the same, the central optical depths of the components are related as

$$\frac{\tau_1}{\tau_2} = \frac{\lambda_1}{\lambda_2} \frac{f_1}{f_2} \qquad (10)$$

where the indices 1 and 2 again apply to the principal and secondary doublet line. Consequently, using Eqs. (5), (6), (8) and (10), discrete absorption components of a resonance doublet in a spectrum normalized at unity can be modelled as

$$
\begin{aligned}
I(v) &= \exp(-\tau_1 \phi_1(v) - \tau_2 \phi_2(v)) \\
&= \exp\left\{ -\tau_c \exp\left[-\left\{ \frac{v - v_c}{v_t} \right\}^2 \right] \right\} \cdot \\
&\quad \cdot \exp\left\{ -\tau_c \frac{\lambda_2}{\lambda_1} \frac{f_2}{f_1} \exp\left[-\left(\frac{v - v_c - v_{split}}{v_t} \right)^2 \right] \right\}, \quad (11)
\end{aligned}
$$

which is a model with three free parameters, τ_c, v_c and v_t, now referring to the line profile parameters of the principal doublet line. Models for multiple DACs are obtained by multiplying as many of the expressions in Eq. (11) as DACs are present in the spectrum:

$$I(v) = I_1(v) \cdot I_2(v) \cdot \dots \cdot I_{N_{DAC}}(v) \qquad (12)$$

where N_{DAC} is the number of DACs to be modelled. Hence, the number of free parameters in a model for multiple DACs equals three times the number of DACs that are modelled.

Before we compared the theoretical profile (Eq. 12) with the reduced spectra of γ Cas, we first convolved the theoretical profile with the instrumental profile which is assumed to have a Gaussian shape with FWHM = 3 pixels (each pixel corresponds to a velocity range of 7.7 km/s, see Turnrose and Thompson 1984). We used this instrumental profile for images obtained with both small and large aperture, since the resulting point spread function of the SWP camera with either of these apertures is practically the same (see Turnrose and Thompson 1984). Then we rebinned the convolved theoretical spectrum similarly to the spectrum extraction routine in the IUEDR reduction program. This routine effectively rebins spectra on a grid with 1.414 times the pixel width. Finally the model spectrum was mapped to a uniform wavelength grid with 0.1 Å sample width. We used the resulting profile as a model for DACs in a quotient spectrum.

4.2. Fitting the model

We fitted the model to the quotient spectra spectra of γ Cas at wavelength regions around the resonance doublets of N V, Si IV and C IV. Fits were attempted on absorption features that exceed the average noise level. Since, for a given spectrum, DACs in lines of different ions tend to appear at more or less the same velocity, we could facilitate the identification of small absorption enhancements by overplotting the three doublets on a velocity scale. When no indication of extra absorption in the normalized spectra was found, no fit was attempted. When multiple DACs were apparent in the spectra, we applied a model containing multiple exponential Gaussians. We fitted our model to spectral data within the velocity range -2500 km/s to $+2500$ km/s (relative to the principal doublet line). This implies that the model is fitted to 207 data points in the case of the N V doublet, to 232 data points in the Si IV doublet region and to 258 data points in the spectral region around the C IV doublet. Since signal to noise estimates of the spectra are available (see previous section), we used the χ^2 criterion to find the best model parameters for the observed absorption features. We used these parameters to calculate the column density (Eq. 9) corresponding to the absorption features. The laboratory wavelengths and the oscillator strengths of the doublets are given in Table 2.

We coded the fit routine using the Marquardt method as described by Press et al. (1986). The number of degrees of freedom is $207 - 3N_{DAC}$, $232 - 3N_{DAC}$ and $258 - 3N_{DAC}$ for the N V, Si IV and C IV doublet respectively.

Using the χ^2 method implies that formal errors on the derived values of the line-profile parameters v_c, τ_c and v_t, can be derived. We used these formal errors to calculate the standard deviation of the column density, $\sigma_{N_{col}}$, of the modelled absorption components:

$$
\begin{aligned}
\frac{\left(\sigma_{N_{col}} \right)^2}{N_{col}^2} &= \sigma_{\tau_c}^2 + \sigma_{v_t}^2 + \frac{2\Delta^2(v_t, \tau_c)}{v_t \tau_c} \\
&\quad + \left(\frac{\sigma_{v_c}}{v_c + c} \right)^2 - \frac{2\Delta^2(v_t, v_c)}{v_t(v_c + c)} - \frac{2\Delta^2(\tau_c, v_c)}{\tau_c(v_c + c)} \quad (13)
\end{aligned}
$$

where σ_{τ_c}, σ_{v_t}, and σ_{v_c} are the derived errors on parameters τ_c, v_t, and v_c respectively. Symbols $\Delta^2(x, y)$ denote the covariance of x and y. Only the first three terms on the right hand side of Eq. (13) contribute significantly to the error on the column density.

Figure 4 shows examples of the residual spectra at two different epochs. We see that the spectra are well normalized and that the models fit satisfactorily. Table 4 lists, for all spectra to which fits were made, the fitted line profile parameters, v_c, τ_c, and v_t and the reduced χ^2 value. Velocities v_c and v_t are given in km/s. Table 4 also lists the values of the derived column densities, N_{col}, in units of $10^{13} cm^{-2}$. All errors in this table are 1σ errors. Considering the χ^2 values of Table 4, we conclude that the normalization procedure we used serves the aim of fitting DAC models very well.

For a few spectra, however, badly normalized continuum regions caused the fitting routine to find components with very
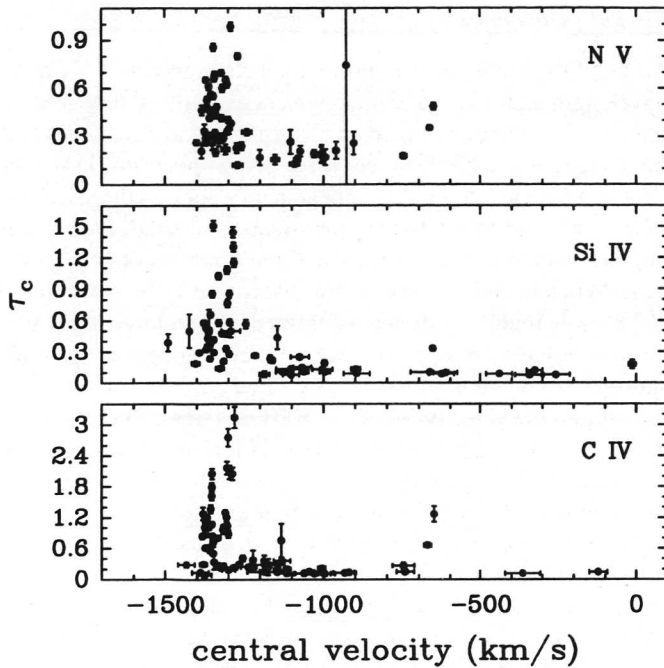
Fig. 5. Top) The derived central optical depth, τ_c, of an absorption component in the N V wavelength region as a function of its central velocity, v_c. Error bars indicate 1σ errors. **Middle)** As Top) for DACs in the Si IV region. **Bottom)** As Top) for DACs in the C IV region

Fig. 6. As Fig. 5, but for the derived broadening parameter, v_t

large broadening parameters, $v_t > 1000$ km/s. We did not include these results in Table 4. The spectra for which these problems occurred are: SWP1449, SWP14274, SWP14430, SWP15702 and SWP21581.

While fitting the models we found minor absorption contributions in three of the spectra we used to create our template spectrum: SWP17979, SWP18136 and SWP18206. However, these DACs are too small to affect the template spectrum significantly, and therefore we did not reconstruct our template.

5. Properties of DACs in the spectra of γ Cas

Below we summarize the results obtained from the modelling procedure described in the previous section. The derived properties of DACs in the spectra of γ Cas, as listed in Table 4, are consistent with the results of Henrichs et al. (1983). Since we used improved IUE data reduction methods (see Sect. 3) and applied error estimates (Fig. 3) to the fitting routine, the uncertainties in our results are considerably smaller than those given by Henrichs et al.

– We find DACs in 62 out of 133 UV spectra of γ Cas. In 40 spectra DACs appear in all three considered doublets. In 17 spectra multiple components are present in one or more of the three doublets. We find a total number of DACs of 62, 62, and 74 in the wavelength regions around the N V, the Si IV and the C IV doublet respectively.

– The vast majority of the DACs have a central velocity, relative to the stellar rest frame, in the range -900 to -1500 km/s. Errors in the central velocities of individual DACs are typically in the order of 1%. In 38 spectra we find 41 sets of three matching components, i.e. a DAC in each of the considered doublets at practically the same velocity. The mean central velocity of each of these sets of 3 DACs has a 1σ error of less than 20 km/s.
– The central optical depth of the components varies from the detection limit (≈ 0.15) up to approximately $\tau_c=1.0$, $\tau_c=1.5$, and $\tau_c=3.2$ for the N V, Si IV, and C IV doublet respectively. Figure 5 shows that these high values are only reached by DACs at outflow velocities larger than 1200 km/s. We find maximum optical depth at approximately -1300 km/s.
– Whereas DACs are usually described as narrow components, the large range in derived values (up to 600 km/s) and the distribution of the broadening parameter v_t (see Fig. 6) indicate that a distinction can be made between narrow and broad components. We adopt an arbitrary discriminative value of 250 km/s for narrow components.
Broad components are mostly found in the Si IV and C IV doublets; we find only one such DAC in the N V doublet region. Narrow components have a tendency to appear at outflow velocities exceeding 900 km/s. About 50% of the broad components in Si IV is found at outflow velocities less than 900 km/s. A typical 1σ error value for the broadening parameter of narrow components is 10 km/s. Errors in v_t of
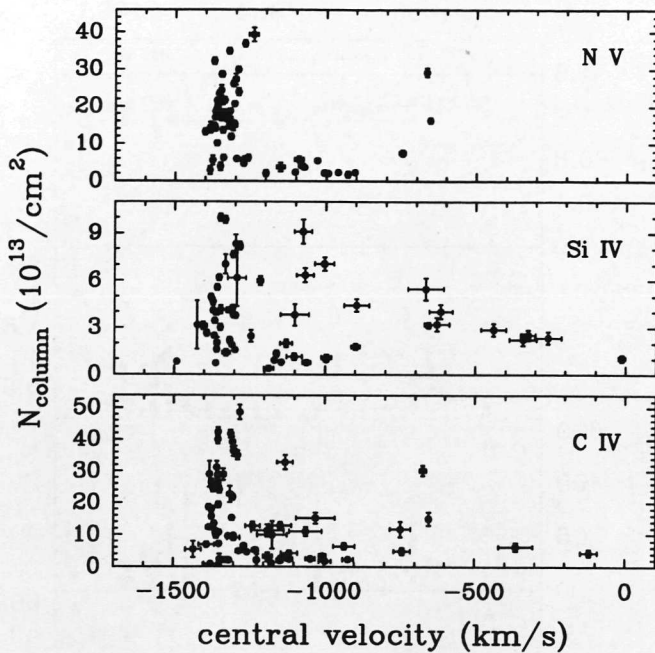
Fig. 7. As Fig. 5, but for the derived column density, N_{col}

broad DACs are usually larger than 30 km/s. In the figures broad components can be identified by their relatively large uncertainty in v_c.

– The highest column densities we derive are $N_{col} \approx 40 \cdot 10^{13} cm^{-2}$, $N_{col} \approx 10 \cdot 10^{13} cm^{-2}$, and $N_{col} \approx 49 \cdot 10^{13} cm^{-2}$ for the N V, Si IV, and C IV doublet respectively. Figure 7 displays the column density of the DACs as a function of their central velocity. This figure clearly shows that narrow components (which have small error bars) fill only a restricted area in the N_{col} versus v_c diagrams. Maximum values of N_{col} are found at approximately -1300 km/s. Narrow components with outflow velocities less than approximately 1200 km/s mostly have relatively small column densities, i.e. $N_{col} < 8 \times 10^{13} cm^{-2}$ for the N V and C IV doublet and $N_{col} < 3 \times 10^{13} cm^{-2}$ for the Si IV doublet.

Kaper et al. (1992) showed that for O stars single DACs follow tracks through a N_{col} versus v_c diagram. Low-velocity broad DACs gradually evolve into high-velocity narrow DACs. With increasing central velocity the column density first increases, then peaks at approximately 0.75 times the terminal velocity and thereafter decreases to the detection level as the DACs almost reach the terminal velocity of the O-star wind. Henrichs et al. (1983) apparently found the high-velocity part of such a DAC evolution in the case of γ Cas . Although the time resolution of the spectra of γ Cas we used did not allow monitoring one single DAC in time, we find that the results as presented in Fig. 7 are consistent with the findings of Kaper et al. (1992) for O stars.
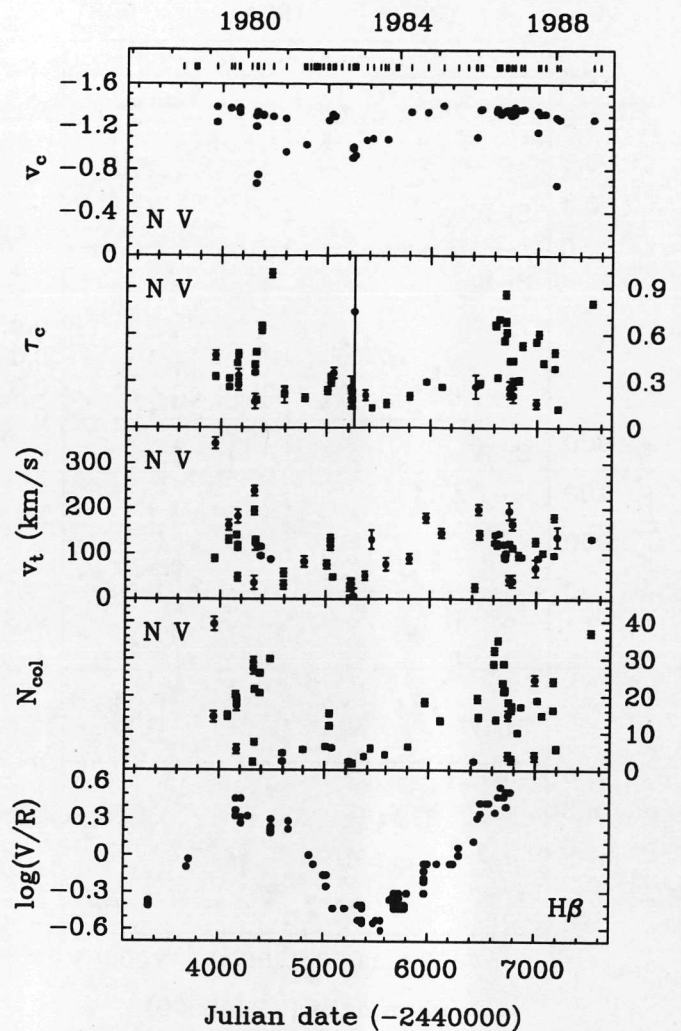
Fig. 8. Properties of DACs detected in the N V doublet region of γ Cas as a function of time. Error bars indicate 1σ errors. From top to bottom: — IUE spectrum acquisition times — The central velocity v_c of the components, in 10^3 km/s — The central optical depth τ_c of the components — The width v_t of the DACs — The derived column density N_{col} of the components — The ^{10}log of the V/R variation of the Balmer Hβ emission line (data from Cowley et al. 1976 and Doazan et al. 1987)

6. DACs and V/R variability of γ Cas

We have investigated the possible existence of a correlation between the DAC behaviour and the Hβ V/R variability of γ Cas. In Figs. 8–11 we present the variations of DAC properties as a function of time. In the top panel of these figures the acquisition dates of all 133 IUE images are marked, including the spectra in which no DACs were found. The Hβ V/R variation is displayed in the bottom panel of these figures.

The variability of components seen in the N V doublet region is given in Fig. 8. The deduced DAC model parameters, v_c, τ_c, and v_t, as well as the derived column densities, are plotted as a function of time. Figures 9 and 10 give the same information,
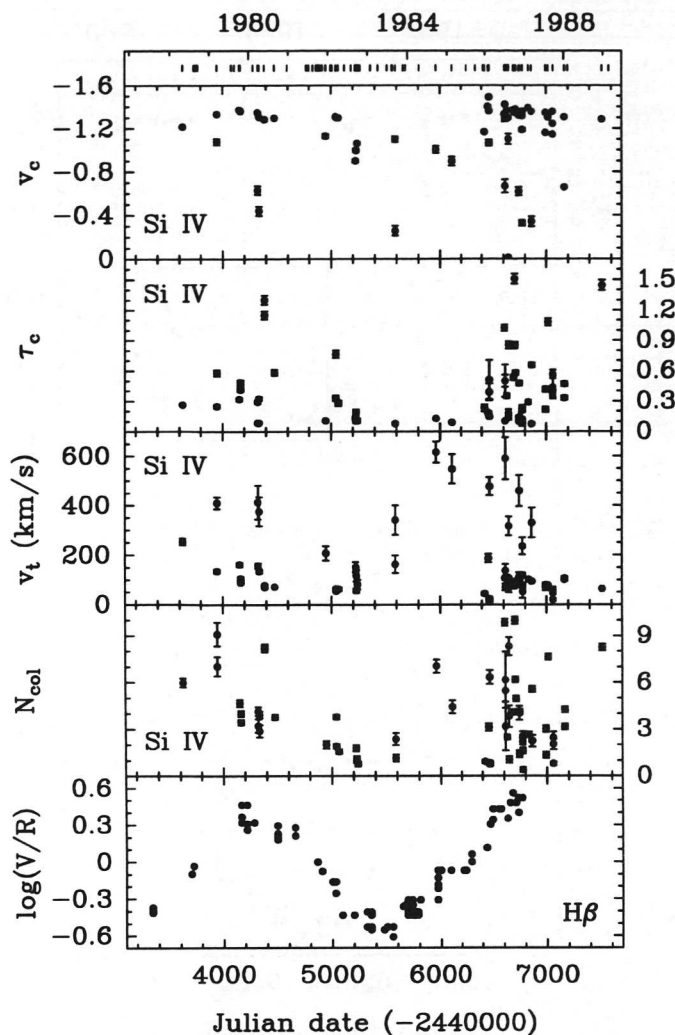
Fig. 9. As Figure 8, for DACs detected in the Si IV doublet region
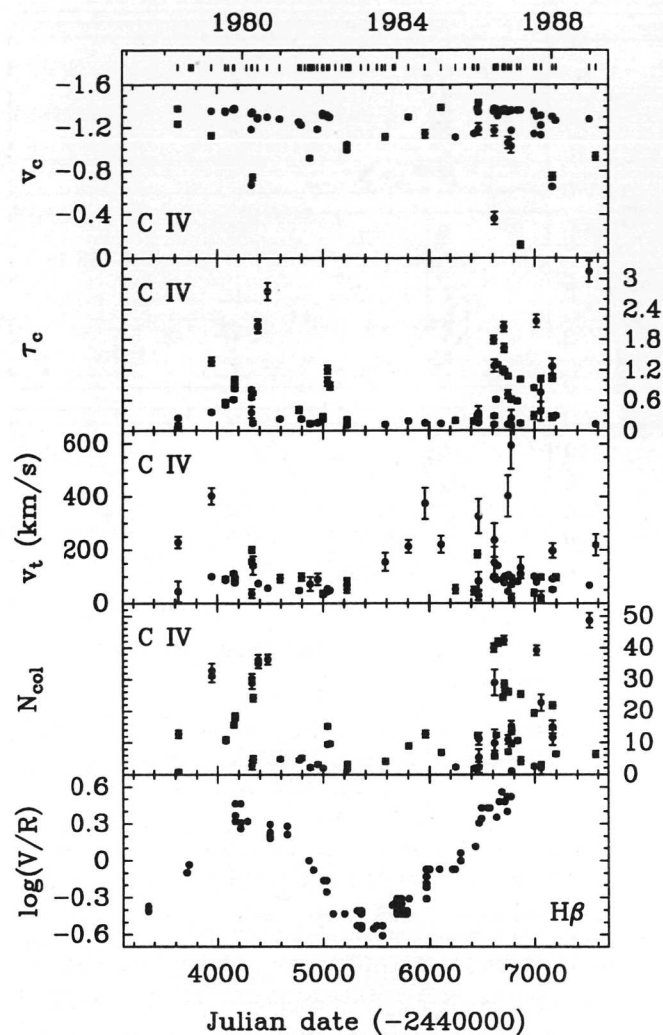
Fig. 10. As Figure 8, for DACs detected in the C IV doublet region

but based on the DACs detected in the Si IV and C IV regions respectively.

It appears from these figures that the DAC behaviour and the V/R variations of γ Cas are correlated. To quantify this correlation we chose to compare the mean values of DAC parameters for phases of V>R with those for phases of V<R. The bottom panel of Fig. 11 gives the complete V/R history of the Hβ emission line from 1969 to 1989. We fitted a function with six parameters to these data. This function has the form

$$\log(V/R) = A + (B + Ct)\sin\left\{2\pi\frac{t-F}{D+Et}\right\}, \quad (14)$$

where parameter t denotes the time in JD. We assumed a constant relative error for the values of V/R, and scaled this error to get the reduced $\chi^2=1$. From the fit we find $A = -0.006 \pm 0.014$, $B = 0.297 \pm 0.035$, $C = 0.0000345 \pm 0.0000077$, $D = 1735 \pm 21$, $E = 0.206 \pm 0.015$, and $F = 6165 \pm 27$. According to the fit both the period and the amplitude of the V/R cycle

increase with time. We used this function to find time intervals with V>R and with V<R.

In Table 3 we present the mean DAC characteristics for phases of V>R and phases of V<R. The bottom section of this table lists average values of the deduced model parameters, v_c, τ_c, and v_t, and of N_{col} of the DACs detected in each of these V/R phases. These quantities are listed for each of the doublets. We also list these quantities for a selection of all detected DACs, namely those with the largest outflow velocity in any of the doublets (top-velocity DAC). In Fig. 11a we show for this selection of DACs the central velocity as a function of time.

From Figs. 8–11 and Tables 3 and 4 we derive the following conclusions:

1. We confirm the finding of Doazan et al. (1987): there are significantly more DACs in phases of V>R than in phases of V<R. We find an average number of DACs of 2.6 per

		V>R	V<R
Number of IUE spectra		21+37 = 58	1+74 = 75
Total number of DACs		52+101 = 153	3+42 = 45
Mean number of DACs per spectrum		2.6	0.6
Number of DACs in N V region		47	15
Number of DACs in Si IV region		49	13
Number of DACs in C IV region		57	17
N V doublet	Average v_c	−1268.2 ± 25.7	−1156.0 ± 44.0
	Average v_t	119.8 ± 8.4	78.8 ± 13.3
	Average τ_c	0.424 ± 0.029	0.268 ± 0.038
	Average N_{col}	17.62 ± 1.42	6.77 ± 1.38
Si IV doublet	Average v_c	−1168.1 ± 48.3	−1035.9 ± 76.3
	Average v_t	146.2 ± 19.1	209.1 ± 51.8
	Average τ_c	0.461 ± 0.051	0.204 ± 0.052
	Average N_{col}	4.16 ± 0.37	2.68 ± 0.56
C IV doublet	Average v_c	−1207.1 ± 34.5	−1212.5 ± 35.8
	Average v_t	119.8 ± 13.5	109.4 ± 23.2
	Average τ_c	0.812 ± 0.092	0.325 ± 0.083
	Average N_{col}	17.38 ± 1.70	5.92 ± 1.13
Top velocities	Average v_c	−1328.5 ± 14.6	−1179.9 ± 35.5
	Average v_t	96.3 ± 6.5	74.5 ± 9.7
	Average τ_c	0.650 ± 0.089	0.291 ± 0.052
	Average N_{col}	13.44 ± 1.83	5.21 ± 0.98

Table 3. Top section: Distribution of spectra and detected DACs for time intervals with V>R and time intervals with V<R. The IUE data range coincides with two phases of V>R and two phases of V<R. Numbers of each of these 4 phases are listed separately in the first two rows of the table. Note the difference in the mean number of DACs per spectrum. **Bottom section:** Average values of parameters of DACs as a function of the V/R phase. These averages are computed for each of the three doublets separately and also for the selection of DACs as displayed in Fig. 11a (top-velocity DACs, see text). Error values denote 1σ errors in mean. Note the difference of the mean values of τ_c (significant) and N_{col} (factor of 2) in each of the V/R phases. The mean central velocity of the top-velocity DACs differs significantly from phase to phase.
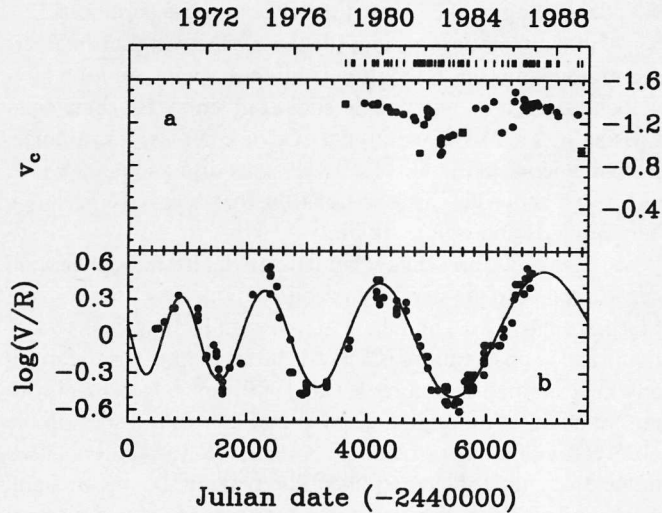
Fig. 11. a) Selection of fastest DACs per SWP spectrum. Units are 10^3 km/s. **b)** Observed V/R variability of the Hβ line with fitted function. Error bars denote 1σ errors

the C IV doublet respectively. The average central optical depths of the DACs detected in the N V and Si IV doublet regions in phases of V<R indicate that these components are just deeper than noise dips, which can have values up to $\tau_c \sim 0.15$ (see Fig. 4).

3. The average highest central velocity of the DACs is significantly higher in phases of V>R than in phases of V<R.

4. We have computed the ratios of column densities of 41 sets of three matching components, i.e. components appearing in three doublets at practically equal velocities. We find that the ratio of column density of DACs detected in different doublet regions is varying with time. However, there is no obvious correlation between the variation in these ratios and the V/R variability.

We can understand the first three conclusions if we assume that (1) the outflowing structures in the stellar wind of γ Cas, which we detect as DACs in UV resonance lines, have higher (column) densities when V/R>1 than when V/R<1 (Table 3) and that (2) the optical depth of these structures decreases as they move away from the star (as a result of geometrical expansion). Then we expect to find

− more DACs in phases of V>R, since the relatively high density of matter in the outflowing structures in these phases enables us to detect them more easily than during phases of V<R (1),

− stronger components in phases of V>R (1),

− lower average outflow velocities when the column densities are low, i.e. in phases of V<R, since beyond a certain distance from the star the structures are not dense enough to produce detectable absorption components (1 and 2),

which is in accordance with what is observed. A consequence of assumption (2) is that the derived outflow velocities of DACs

spectrum for phases of V>R, and of 0.6 per spectrum for phases of V<R.

2. DACs occurring in the N V, C IV, and, to a lesser extent, the Si IV, doublet have higher column densities in phases of V>R than in phases of V<R. This is primarily due to significantly larger values of the central optical depth of components in phases of V>R than in phases of V<R. The mean column density of DACs found in the N V doublet is 2.6 ± 0.6 times higher in the former than in the latter phase. This number is 1.6 ± 0.4 and 2.9 ± 0.6 for the Si IV and

are always a lower limit for the terminal velocity, v_∞, of the wind. Assumption (2) is also made by Kaper et al. (1992) to explain the tracks that DACs follow in a N_{col} versus v_c diagram.

7. Discussion

We have found strong evidence for a correlation between variations in V/R ratio and DAC behaviour. During 11 years the Hβ V/R ratio and the DAC variability of γ Cas exhibited a similar periodicity. The V/R variation of γ Cas is believed to have its origin in an equatorial disc around the star. The Balmer emission lines are primarily formed by recombination in ionized regions of this high-density low-velocity wind. Since the strength of the emission lines depends on the density squared, we expect the regions of the wind closest to the star to contribute most to the emission strength if the density of the equatorial wind decreases outwards. IR observations of γ Cas revealed that this is indeed the case. The correlation between the V/R variability and the strength of DACs might therefore indicate that the structures in the high-velocity wind of γ Cas start their outflowing motion close to the star.

In our picture the V/R variability is caused by the revolution of a non-axisymmetric equatorial disc-like wind (Telting et al. 1993). If the asymmetrical structure of this disc rotates around the star, we expect V/R variation on the time scale of this rotation. The disc can have a non-axisymmetrical shape due to, for example, tidal interaction with a companion star (e.g. Cowley and Gugula 1973). However, there is no direct evidence for the existence of a companion of γ Cas. Indirect evidence comes from the X-ray luminosity of γ Cas. In 1976 γ Cas was identified as the optical counterpart of the low-luminosity, variable hard X-ray source MX 0053+604 (Jernigan 1976, Mason et al. 1976). The X-ray spectrum of γ Cas is very similar to that of the X-ray pulsar X Per/4U 0352+30, which is known to be a Be star plus a neutron star in a (probably) wide orbit (White et al., 1982). No X-ray pulsation period has been found for γ Cas, and no orbit can be determined, but in analogy with X Per the orbital period of a possible companion may well be in the order of years. However, if a binary companion would be directly responsible for the V/R variability, we would expect a strict periodicity, which is not observed (Fig. 11).

Another cause for a non-axisymmetrical shape of the disc is an one-armed global normal mode of the disc (Okazaki 1991, Papaloizou et al. 1992, Savonije and Heemskerk 1993). The drastic change in period of the V/R cycles (see Fig. 11) and the time scale of the V/R variation makes this cause of asymmetry the more favourable one. Okazaki found that for a disc with a large radius the rotation period of the $m = 1$ mode is larger than for a small disc. This is consistent with the observed increase of the visual and IR flux of γ Cas and the increasing period of the V/R variation. Papaloizou et al. found that due to the gravitational potential of an oblate star, oscillations on time scales of V/R variations can exist in the disc. In the case of a one-armed oscillation of the equatorial disc, the wind particles in the high-density part of the wave pattern are moving towards

us in phases of V>R, and are moving away from us in phases of V<R (see Fig. 12).

Figures 8–10 clearly show that in phases of V>R the column densities of detected DACs are much larger than in phases of V<R. This is consistent with a model in which the wind structures that cause DACs are formed near the stellar surface in an interacting region of the high-velocity polar wind and the low-velocity equatorial wind of γ Cas, and travel around the star over an azimuthal angle $\phi \sim 90°$ before they reach their final velocity, which is directed radially away from the star (see Fig. 12). We expect that these structures will have relatively high densities if they are formed near regions of the equatorial disc where the density is high, i.e. the region of the disc coming towards us in phases of V>R. Consequently, strong DACs will be found only in phases of V>R, since only then structures formed in high-density regions will end up in the line of sight. Structures formed near the high-density part of the equatorial disc will either miss or relatively rapidly cross the line of sight if they are formed at other epochs in the V/R cycle.

There might be a phase lag between the V/R variation and the observed highest velocity reached by the DACs, the latter probably related to the strength of the DACs (see Fig. 11). This can be explained by adopting a value of ϕ larger or smaller than 90°, depending on the phase difference of these variations.

A theoretical background for the existence of an interacting region between the high-velocity polar wind and the low-velocity equatorial wind of Be stars is given by Bjorkman and Cassinelli (1993). Observational evidence comes, for instance, from the deduced radial velocity laws for disc and polar winds of Be stars and in the case of γ Cas from the observed correlation between V/R and DAC variability.

In Fig. 12 we present a schematic model for the stellar wind of γ Cas close to the star. From detailed modelling Poeckert and Marlborough (1978) find that γ Cas has an inclination $i \sim 45°$. Polarization observations (Clarke 1990) and optical interferometry measurements (Mourard et al. 1989) are in agreement with this value of i. Although the star is inclined with respect to the observer we find a correlation between V/R variability caused in the disc and DAC variations of the wind in the line of sight. This indicates that the structures that form DACs can travel through the polar wind with significant velocity components directed away from the equatorial plane, which means that they do not follow the trajectories of the polar wind. For comparison we plotted in Fig. 12 the trajectories of free polar wind particles in the equatorial plane (dashed curves), ignoring the presence of the disc. We assumed conservation of angular momentum ($i=45°$, $v\sin i=230$ km/s) and a radial velocity distribution

$$v_r(r) = v_0 + (v_\infty - v_0)(1 - R_*/r)^\beta \ ,\qquad (15)$$

where $v_0=10$ km/s is approximately half the sound speed at the surface of γ Cas, $v_\infty \sim 1600$ km/s is the terminal velocity of the wind and $\beta=0.8$.

A one-armed mode moving through the equatorial disc could have further implications. Due to the growth of the disc, the revolution period of the mode and its amplitude increase
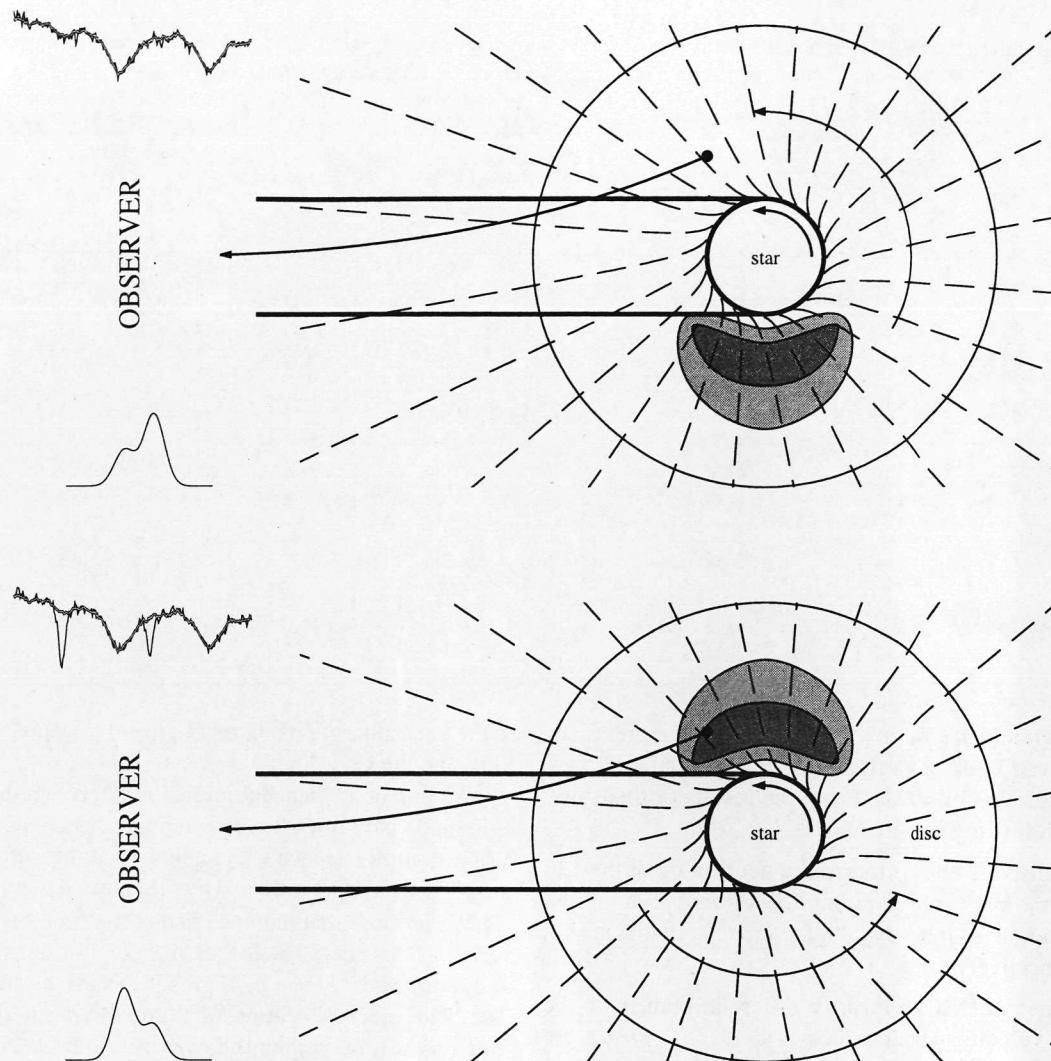
Fig. 12. Schematic model for V/R variations and DACs in spectra of γ Cas. We show a projection of the equatorial and polar winds onto the equatorial plane. The grey areas in the disc represent the high-density part of a one-armed oscillation of the disc. This high-density part revolves around the star on the time scale of the V/R variations of the Balmer lines. The dashed lines are trajectories of individual free stellar wind particles, based on a beta law for the radial velocity (i.e. the polar wind). These trajectories are calculated using Eq. (15) and parameters given in the text. The solid curve represents the path of a density enhancement of the polar wind, as is suggested by comparison of V/R variations and DAC variability. The structure starts off close to the star, near the equatorial plane, and gradually moves away from the star. Its trajectory will be ruled by the motions in the wind: outflow and rotation. Only for a particular azimuthal start-off position the structure ends up in the line of sight, where it can cause a DAC if its density is high enough.   **Top)** The high-density part of the equatorial disc moves away from the observer; the emission lines have V<R. Structures of the fast polar wind that end up in the line of sight are formed near the low-density part of the equatorial disc: DACs are weak (or too weak to be detected).   **Bottom)** The high-density part of the equatorial disc moves towards the observer; the emission lines have V>R. Now the structures of the polar wind travelling to the line of sight are formed near the high-density part of the equatorial disc: the observer finds numerous (strong) DACs

(Fig. 11). If eventually the mode becomes unstable this could result in the collapse of the equatorial disc, as is suggested by the drastic line and continuum variations of γ Cas in 1935–1941 (Goraya and Tur 1988). A "normal" B-type star is what is left over from the original Be star, which will develop a new equatorial disc during the following years (Bjorkman and Cassinelli

1993). If this scenario applies to the history of γ Cas, this could well be the explanation of the Be-phenomenon.

8. Summary and conclusions

We analysed 133 high-dispersion archival IUE spectra of γ Cassiopeiae taken over a period of eleven years and modelled the discrete absorption components which appear in the N v,

Table 4. Results of fitting the model to residual spectra of γ Cas. Fits were made to normalized data at the spectral regions around the N V, Si IV and C IV resonance doublets. The first column gives the SWP image number of each spectrum on which a fit was made. For each doublet the parameters of the best-fitting (multiple) DAC model, v_c, τ_c, v_t, and the derived column densities, N_{col}, are listed. The column density is given in units of 10^{13}cm^{-2}. Velocities v_c and v_t are given in units of km/s. For each doublet the fifth column lists the reduced χ^2 value of the best fit. All quoted errors are 1 σ errors.

SWP image	N V v_c	τ_c	v_t	N_{col}	χ^2	Si IV v_c	τ_c	v_t	N_{col}	χ^2	C IV v_c	τ_c	v_t	N_{col}	χ^2
1449						-1215.8	0.263	253.4	5.98	1.95	-1375.8	0.087	44.3	0.88	0.83
						±9.6	0.013	13.4	0.28		±22.0	0.056	38.5	0.79	
											-1236.4	0.246	227.9	12.77	
											24.3	0.027	21.8	1.23	
4640	-1384.2	0.464	89.3	14.38	2.08	-1330.9	0.579	135.2	7.04	2.33	-1355.9	1.366	100.1	31.18	1.11
	±3.9	0.030	7.2	1.48		4.4	0.031	8.2	0.62		3.5	0.084	5.8	2.01	
	-1240.9	0.328	344.9	39.34		-1074.7	0.248	410.2	9.11		-1130.4	0.358	402.0	32.81	
	15.5	0.019	12.8	1.89		28.5	0.017	23.4	0.77		26.3	0.034	31.0	2.24	
5928	-1371.5	0.317	130.6	14.39	1.57						-1348.3	0.507	92.6	10.72	2.07
	6.1	0.018	8.5	0.81							5.0	0.039	6.8	0.70	
5929	-1372.8	0.261	162.7	14.77	1.48						-1358.4	0.559	87.5	11.15	1.45
	8.2	0.016	11.4	0.89							4.6	0.043	6.2	0.71	
6786	-1359.2	0.415	140.9	20.31	1.83	-1371.3	0.320	162.2	4.67	1.98	-1373.2	0.614	112.3	15.73	1.65
	4.9	0.017	6.7	0.84		6.4	0.016	9.1	0.22		4.8	0.037	6.3	0.81	
6902	-1366.1	0.478	112.5	18.69	1.95	-1358.4	0.415	106.8	3.99	2.11	-1372.6	0.874	91.5	18.23	1.18
	3.8	0.019	5.3	0.75		4.2	0.022	6.0	0.19		3.4	0.048	4.4	0.82	
6903	-1359.7	0.467	119.5	19.36	1.37	-1365.8	0.430	89.0	3.44	1.52	-1382.6	0.838	97.5	18.64	1.35
	4.0	0.018	5.6	0.77		3.8	0.024	5.4	0.17		3.5	0.047	4.6	0.84	

Si IV, and C IV doublets. We investigated possible correlations between observed DAC properties and the observed V/R variability of the Hβ line of γ Cas. From the results of this study we derive the following conclusions.

We detect discrete absorption components in 62 of the 133 analysed spectra. In 17 spectra multiple DACs are present. The number of components in the N V, Si IV, and C IV doublet is 62, 62, and 74 respectively.

In many spectra DACs appear in different doublets at the same outflow velocity which indicates that these DACs are formed by absorption of stellar photons in one particular outflowing high-density wind structure.

In our data set the maximum outflow velocity of a DAC is approximately 1500 km/s. This value can be considered as a lower limit of the terminal velocity of the high-velocity low-density "polar" wind of γ Cas.

We find upper limits of the column densities of DACs of $N_{col} \approx 40 \times 10^{13}$cm^{-2}, $N_{col} \approx 10 \times 10^{13}$cm^{-2}, and $N_{col} \approx 49 \times 10^{13}$cm^{-2} for the N V, Si IV, and C IV doublet respectively. The components occupy only restricted areas in a column density versus central velocity diagram.

We confirm the previously found (Doazan et al. 1987) correlation between the V/R variability of the Hβ line and the presence of DACs in the UV spectra. Significantly more discrete absorption components are seen in phases of V>R than in phases of V<R. The average number of DACs per spectrum, i.e. all three doublets considered, is 2.6 for phases of V>R, and 0.6 for phases of V<R. This is due to the fact that the wind structures responsible for the absorption components have significant higher column densities in phases of V>R than in phases of V<R. The mean column density of DACs found in the N V doublet is 2.6±0.4 times higher in the former than

in the latter phase. This number is 1.6±0.4 and 2.9±0.6 for the Si IV and the C IV doublet respectively.

We find no evidence for a relation between the ratios of the column density of DACs detected in different doublets and the V/R variability. Hence we conclude that the ionization state of the polar wind is not affected by the cause of the V/R variability.

We propose that the observed correlation between the V/R variation and the variation of the column densities of DACs is due to the presence of a global density perturbation in the disc. The precise location of the revolving perturbation as a function of time is then the cause of both quasi-periodic V/R and quasi-periodic DAC variability.

References

Abbott, D.C. 1982 ApJ, 259, 282
Barker, P.K. 1984, ApJ, 89, 899
Bianchi, L., Bohlin, R.C. 1984, A&A, 134, 31
Bjorkman, J.E., Cassinelli, J.P. 1993, ApJ, 409, 429
Boggess, A., et al. 1978a, Nat, 275, 372
Boggess, A., et al. 1987b, Nat, 275, 377
Caroff, L.J., Noerdlinger, D., Scargle, J.D. 1972, ApJ, 176, 439
Clarke, D. 1990, A&A, 227, 151
Coté, J., Waters, L.B.F.M. 1987, A&A, 176, 93
Cowley, A.P., Gugula, E. 1973, A&A, 22, 203
Cowley, A.P., Rogers, L., Hutchings, J.B. 1976, PASP, 88, 911
Dachs, J., Hanuschik, R., Kaiser, D., Rohe, D. 1986, A&A, 159, 276

Table 4. Continued

SWP image	N V v_c	τ_c	v_t	N_{col}	χ^2	Si IV v_c	τ_c	v_t	N_{col}	χ^2	C IV v_c	τ_c	v_t	N_{col}	χ^2
6904	−1375.9	0.334	48.1	5.58	1.43	−1363.0	0.486	91.5	3.99	1.73	−1374.1	1.011	78.0	17.98	1.25
	4.2	0.043	8.7	1.25		3.4	0.024	4.9	0.18		2.8	0.058	3.7	0.81	
	−1329.4	0.274	182.1	17.35											
	10.9	0.035	15.0	1.48											
8554	−1300.3	0.405	194.3	27.32	1.48	−1346.2	0.293	158.0	4.15	1.57	−1334.2	0.807	157.3	28.95	1.07
	8.8	0.019	8.9	1.46		7.4	0.017	10.6	0.27		9.6	0.040	9.1	1.88	
	~1199.9	0.169	35.9	2.11		−628.3	0.087	413.2	3.22		−1186.7	0.358	36.7	3.00	
	7.5	0.048	14.8	0.80		41.1	0.010	68.7	0.43		8.0	0.110	16.3	1.38	
	−666.5	0.353	238.9	29.24							−672.5	0.661	201.4	30.28	
	7.6	0.013	11.3	1.18							10.9	0.045	11.4	1.61	
8666	−1336.9	0.485	129.2	21.74	1.19	−1306.3	0.324	135.0	3.93	1.19	−1347.2	0.747	142.1	24.21	1.01
	3.9	0.018	5.6	0.80		5.9	0.018	8.3	0.21		5.2	0.037	6.1	1.05	
	−747.8	0.178	122.1	7.53		−439.4	0.086	375.5	2.88		−742.7	0.150	142.6	4.86	
	10.3	0.018	14.9	0.77		41.5	0.011	58.1	0.39		27.8	0.037	34.9	1.11	
9129	−1307.9	0.654	115.3	26.18	2.21	−1284.7	1.301	70.8	8.27	2.11	−1287.1	2.052	74.9	35.05	1.37
	2.9	0.020	4.0	0.78		1.4	0.044	2.0	0.21		2.0	0.123	2.7	1.46	
9130	−1303.9	0.628	95.2	20.76	1.51	−1283.1	1.152	79.0	8.17	2.12	−1296.1	2.081	76.4	36.24	0.96
	2.7	0.022	3.8	0.70		1.6	0.039	2.2	0.21		2.1	0.131	2.7	1.62	
9897	−1291.7	0.986	87.7	30.01	2.04	−1296.2	0.582	72.2	3.77	1.74	~1300.5	2.755	57.9	36.39	2.01
	1.8	0.027	2.5	0.72		. 2.6	0.029	3.8	0.16		1.5	0.171	1.9	1.59	
10863	−1273.4	0.229	58.2	4.62	1.38						−1281.9	0.231	93.2	4.91	1.35
	6.0	0.030	8.8	0.54							10.2	0.032	14.2	0.64	
	−960.5	0.213	31.5	2.33											
	5.5	0.053	9.6	0.42											
14274											−1255.0	0.413	48.9	4.60	1.00
											5.0	0.059	7.2	0.53	
14430	−1029.5	0.193	82.3	5.50	1.51						−1227.8	0.232	98.7	5.23	0.71
	8.2	0.023	11.7	0.65							10.6	0.033	14.9	0.67	
15119											−920.3	0.138	72.9	2.28	0.80
											18.0	0.045	26.3	0.67	
15702						−1129.4	0.107	208.2	2.01	1.39	−1186.7	0.155	90.4	3.20	0.83
						20.4	0.013	28.8	0.24		15.3	0.034	21.5	0.65	
16157											−1314.9	0.251	36.0	2.06	1.08
											6.2	0.063	9.6	0.39	
16159											−1334.3	0.263	34.7	2.08	1.25
											6.2	0.064	9.7	0.39	
16167											−1323.1	0.240	38.1	2.09	1.25
											6.8	0.060	10.4	0.41	
16284	−1258.6	0.240	76.1	6.35	1.36										
	6.3	0.025	9.0	0.62											
16518	−1303.7	0.330	133.3	15.26	1.31	−1307.7	0.329	64.3	1.90	1.34	−1317.4	0.970	43.1	9.54	1.25
	5.9	0.018	8.2	0.81		4.2	0.028	6.1	0.14		2.3	0.086	3.2	0.60	
16528	−1315.3	0.291	117.3	11.87	1.40	−1303.3	0.765	55.2	3.79	2.02	−1305.8	1.209	55.3	15.26	1.32
	6.4	0.020	9.1	0.78		1.9	0.038	2.7	0.15		2.2	0.082	3.0	0.77	
16694	−1297.1	0.352	48.9	5.98	1.47	−1297.7	0.279	62.9	1.57	1.99	−1299.9	0.883	48.4	9.75	1.92
	3.7	0.035	5.6	0.50		4.8	0.028	7.1	0.14		2.7	0.076	3.6	0.63	
17921	−904.7	0.259	25.9	2.33	0.92	−898.8	0.132	151.4	1.79	1.02					
	4.6	0.072	8.7	0.39		14.2	0.015	20.1	0.20						
17974	−1007.0	0.185	34.2	2.19	0.60	−995.7	0.104	117.3	1.10	1.01	−997.1	0.116	66.8	1.77	0.70
	6.8	0.050	11.2	0.45		16.0	0.018	22.8	0.18		19.8	0.044	28.1	0.61	
17978	−993.7	0.171	34.5	2.05	1.00	−996.9	0.191	56.7	0.97	1.14	−1005.6	0.216	69.3	3.41	0.87
	7.1	0.050	11.8	0.44		6.5	0.028	9.6	0.13		11.5	0.049	16.3	0.67	
17979	−1005.9	0.193	33.1	2.21	0.74						−1045.2	0.153	71.5	2.49	0.81
	± 6.4	0.053	10.8	0.44							± 15.8	0.043	22.5	0.65	
18136						−1061.8	0.106	81.0	0.77	0.91					
						± 13.4	0.022	19.6	0.15						
18206	−928.7	0.744	6.8	1.77	0.74										
	3.9	2.203	17.5	0.79											
19097	−1072.9	0.208	51.2	3.69	0.97										
	6.3	0.033	9.6	0.52											
19656	−1090.5	0.128	130.9	5.84	0.96										
	15.0	0.018	20.9	0.80											
20988	−1082.0	0.156	76.3	4.14	0.94	−1101.9	0.078	163.0	1.14	1.09	−1115.6	0.119	154.4	4.19	0.74
	9.7	0.025	14.3	0.62		25.3	0.015	36.3	0.22		27.1	0.026	33.8	0.84	
						−257.7	0.077	341.0	2.36						
						44.8	0.013	59.7	0.38						
22760	−1340.5	0.203	89.3	6.30	1.28						−1299.4	0.187	212.7	9.07	1.11
	7.7	0.022	11.1	0.65							20.5	0.021	24.1	0.88	
24001	−1338.6	0.294	178.8	18.28	1.06	−1003.5	0.128	616.4	7.06	1.31	−1145.1	0.150	373.9	12.81	0.93
	7.6	0.015	10.7	0.94		31.8	0.008	43.5	0.43		36.4	0.021	58.8	1.16	
25238	−1400.6	0.263	145.1	13.27	1.25	−896.0	0.090	547.5	4.43	1.25	−1389.2	0.138	220.0	6.92	0.97
	7.7	0.017	10.7	0.85		41.7	0.008	59.6	0.41		26.2	0.019	31.8	0.81	
26338											−1114.1	0.197	52.7	2.36	0.77
											10.7	0.051	15.6	0.55	
27391	−1102.9	0.266	26.2	2.42	0.89	−1167.7	0.231	44.2	0.92	1.29	−1146.1	0.183	46.8	1.95	0.97
	4.7	0.074	8.7	0.41		5.2	0.035	7.7	0.12		10.8	0.057	15.7	0.51	

Dachs, J. 1987, in 'Physics of Be stars', IAU Colloquium 92, eds. A. Slettebak and T.P. Snow, Cambridge University Press, p. 150

Doazan, V. 1982, in 'B stars with and without emission lines', eds. A.B. Underhill and V. Doazan, NASA SP-456, p. 325

Doazan, V., Franco, M., Rusconi, L., Sedmak, G., Stalio, R. 1983, A&A, 128, 171

Doazan, V., Rusconi, L., Sedmak, G., Thomas, R.N., Bourdonneau, B. 1987, A&A, 182, L25

Doazan, V., Barylak. M., Rusconi, L., Sedmak, G., Thomas, R.N., Bourdonneau, B. 1989, A&A, 210, 249

Dougherty, S.M., Taylor, A.R. 1992, Nat, 359, 808

Ferlet, R., Laurent, C., Vidal-Madjar, A., York, D.G. 1980, ApJ, 235, 478

Gehrz, R.D., Hackwell, J.A., Jones, T.W. 1974, ApJ, 191, 675

Giddings, J.R. 1983a, ESA IUE Newsletter, 17, 53

Giddings, J.R. 1983b, SERC Starlink User Note, no. 37

Goraya, P.S., Tur, N.S. 1988, Ap&SS, 145, 263

Grady, C.A., Bjorkman, K.S., Snow, T.P. 1987, ApJ, 320, 376

Hammerschlag-Hensberge, G. 1979, IAU Circ. 3391

Henrichs, H.F., Hammerschlag-Hensberge, G., Howarth, I.D., Barr, P. 1983, ApJ, 268, 807

Henrichs, H.F. 1984, in Proceedings of 4th European IUE Conference, ESA SP-218, p. 43

Howarth, I.D., Prinja, R.K. 1989, ApJS, 69, 527

Huang, S.-S. 1972, ApJ, 171, 549

Jernigan, J.C. 1976, IAU Circ. 2900

Kaper, L., Henrichs, H.F., Nichols-Bohlin, J. 1992, in Proc. 'Variable Stars and Galaxies', ASP Conf. Series, Vol. 30, ed. B. Warner, p. 135

Lesh, J.R. 1968, ApJS, 17, 371

Lucy, L.B. 1984, A&A, 140, 210

Marlborough, J.M. 1969, ApJ, 156, 135

Mason, K.O., White, N.E., Sanford, P.W. 1976, Nat, 260, 690

Mourard, D., Bosc, I., Labeyrie, A., Koechlin, L., Saha, S. 1989, Nat, 342, 520

Okazaki, A.T. 1991, PASJ, 43, 75

Papaloizou, J.C., Savonije, G.J., Henrichs, H.F. 1992, A&A, 265, L45

Poeckert, R., Marlborough, J.M. 1978, ApJ, 220, 940

Press, W.H., Flannery, B.P., Teukolsky, S.A., Vetterling, W.T. 1986, 'Numerical recipes', Cambridge University Press

Prinja, R.K. 1989, MNRAS, 241, 721

Savonije, G.J., Heemskerk, M.H.M. 1993, A&A, 276, 409

Secchi, A. 1867, Astron. Nachr., 68, 63

Slettebak, A. 1982, ApJS, 50, 55

Slettebak, A. 1988, PASP, 100, 770

Snow, T.P. 1982, ApJ, 253, L39

Sobolev, V.V. 1960, 'Moving envelopes of stars', Harvard University Press

Taylor, A.R., Waters, L.B.F.M., Lamers, H.J.G.L.M., Persi, P., Bjorkman, K.S. 1987, MNRAS, 228, 811

Telting, J.H., Waters, L.B.F.M., Persi, P., Dunlop, S. 1993, A&A, 270, 355   *Thesis Chapter 2*

Turnrose, B.E., Thompson, R.W. 1984, 'IUE Image Processing Information Manual', version 1.1, CSC/TM-81/6268

Van den Heuvel, E.P.J., Rappaport, S. 1987, in 'Physics of Be stars', IAU Colloquium 92, eds. A. Slettebak and T.P. Snow, Cambridge University Press, p. 291

Waters, L.B.F.M., Coté, J., Lamers, H.J.G.L.M. 1987, A&A, 185, 206

Waters, L.B.F.M., Taylor, A.R., van den Heuvel, E.P.J., Habets, G.M.H.J., Persi, P. 1988, A&A, 198, 200

Waters, L.B.F.M. 1989, in Proc. 23rd ESLAB symposium, Vol. 1: X-ray binaries, eds. J. Hunt and B. Battrick, p. 25

White, N.E., Swank, T.P., Holt, S.S., Parmar, A.N. 1982, ApJ, 263, 277

Table 4. Continued

SWP image	N V v_c	τ_c	v_l	N_{col}	χ^2	Si IV v_c	τ_c	v_l	N_{col}	χ^2	C IV v_c	τ_c	v_l	N_{col}	χ^2
27607	−1362.9	0.280	197.8	19.27	1.54	−1404.1	0.186	187.2	3.13	1.48	−1379.1	0.294	184.1	12.36	1.01
	8.2	0.015	11.8	0.98		11.7	0.015	16.7	0.24		11.7	0.023	14.1	0.85	
27669	−1368.2	0.289	142.4	14.29	1.24	−1491.4	0.389	23.7	0.83	1.68	−1433.4	0.287	83.3	5.45	0.99
	7.0	0.017	9.8	0.85		3.1	0.084	6.1	0.12		26.7	0.049	33.2	2.58	
						−1361.9	0.511	16.1	0.74		−1345.6	0.339	29.4	2.27	
						2.8	0.192	6.4	0.10		7.8	0.139	17.3	1.74	
						−1067.2	0.148	477.1	6.34		−1187.3	0.152	325.4	11.29	
						28.0	0.009	36.5	0.45		53.9	0.024	64.2	1.89	
28555	−1345.0	0.664	124.4	28.69	1.13	−1332.0	1.024	107.3	9.87	1.81	−1352.3	1.795	97.7	40.00	0.95
	2.8	0.019	4.1	0.79		2.0	0.030	2.8	0.23		2.3	0.083	2.9	1.34	
28601	−1371.3	0.653	142.1	32.25	1.18	−1423.7	0.499	71.0	3.18	1.30	−1379.9	1.277	99.8	29.05	1.08
	3.0	0.018	4.3	0.84		6.9	0.159	13.5	1.55		7.4	0.123	7.1	4.11	
						−1292.6	0.499	137.6	6.17		−1172.0	0.286	152.5	9.94	
						29.6	0.059	26.3	1.81		48.7	0.043	57.4	4.28	
						−666.2	0.103	590.9	5.47		−364.1	0.117	236.3	6.26	
						60.2	0.008	85.9	0.69		56.8	0.031	63.3	1.33	
28724	−1342.1	0.325	121.2	13.68	1.02	−1366.9	0.350	79.2	2.49	1.19	−1371.6	0.614	89.0	12.45	1.07
	5.7	0.019	8.1	0.77		4.3	0.025	6.1	0.16		4.3	0.042	5.8	0.72	
28841	−1322.1	0.698	144.2	34.97	1.05	−1297.3	0.853	108.7	8.33	1.23	−1309.7	1.301	140.8	41.78	0.90
	2.9	0.018	4.1	0.86		2.8	0.036	5.3	0.58		3.4	0.048	4.0	1.24	
						−1101.3	0.134	316.4	3.82						
						47.3	0.019	37.4	0.70						
						−13.4	0.178	65.8	1.05						
						11.4	0.041	16.5	0.21						
29269	−1355.1	0.561	120.7	23.50	1.08	−1370.6	0.531	85.8	4.10	1.04	−1367.3	1.198	89.2	24.38	1.07
	3.3	0.019	4.7	0.77		3.1	0.025	4.3	0.17		2.7	0.060	3.5	0.94	
29343	−1346.6	0.857	96.4	28.71	1.08	−1348.1	1.507	73.8	10.00	1.13	−1351.6	2.051	90.7	42.40	1.14
	2.0	0.024	2.9	0.71		1.4	0.050	1.8	0.24		2.1	0.100	2.6	1.50	
29379	−1343.5	0.683	89.4	21.22	0.99	−1351.8	0.853	81.0	6.20	1.15	−1353.0	1.626	77.3	28.65	1.06
	2.4	0.024	3.4	0.68		2.0	0.032	2.8	0.19		2.2	0.085	2.8	1.10	
29416	−1361.8	0.613	101.7	21.65	1.19	−1378.2	0.579	95.4	4.96	1.18	−1373.6	1.159	100.2	26.50	1.43
	2.9	0.021	4.0	0.73		3.0	0.024	4.1	0.18		2.9	0.056	3.8	0.99	
29645	−1350.7	0.260	43.3	3.91	1.20	−1327.4	0.139	111.8	1.40	1.21	−1348.4	0.713	44.2	7.18	1.31
	5.3	0.042	10.8	1.07		12.4	0.019	18.6	0.22		3.3	0.080	5.0	0.70	
	−1308.4	0.220	194.5	14.86		−616.2	0.098	459.7	4.03		−1061.2	0.120	402.3	11.02	
	12.6	0.030	19.0	1.34		38.6	0.009	63.2	0.45		53.8	0.021	78.0	1.41	
29666	−1338.3	0.432	122.6	18.37	1.57	−1320.4	0.476	96.5	4.12	1.31	−1352.2	1.071	106.9	26.12	1.32
	4.3	0.018	6.1	0.77		3.6	0.023	5.0	0.18		3.3	0.051	4.1	1.00	
29848	−1385.0	0.209	40.5	2.94	1.31	−1315.6	0.208	117.7	2.20	1.61	−1357.3	0.619	69.4	9.81	1.24
	6.8	0.045	13.3	1.06		8.3	0.019	11.8	0.19		4.3	0.054	6.5	0.91	
	−1322.4	0.292	165.7	16.78		−325.7	0.120	235.4	2.53		−1028.9	0.113	593.8	15.24	
	10.7	0.030	11.9	1.37		25.4	0.015	34.4	0.33		64.1	0.016	89.6	1.71	
29853	−1347.7	0.432	113.3	16.99	2.02	−1358.6	0.232	77.5	1.62	1.30	−1364.3	0.612	96.9	13.54	1.14
	4.2	0.019	5.9	0.76		7.0	0.025	11.0	0.18		4.5	0.040	6.3	0.76	
						−1186.6	0.083	52.1	0.39		−1174.4	0.245	20.2	1.13	
						16.6	0.030	25.5	0.15		7.7	0.155	14.5	0.39	
30262	−1361.6	0.305	96.2	10.20	1.66	−1392.2	0.290	101.9	2.65	1.35	−1359.6	0.576	81.7	10.73	1.21
	5.5	0.021	7.8	0.69		5.7	0.021	8.2	0.18		4.3	0.044	5.8	0.67	
30445	−1367.6	0.529	93.1	17.11	1.31	−1357.5	0.656	94.5	5.57	1.38	−1361.4	1.010	110.1	25.38	1.39
	3.1	0.022	4.4	0.68		2.7	0.025	3.7	0.19		3.3	0.050	4.4	0.97	
						−342.9	0.076	330.2	2.25		−121.6	0.143	133.2	4.33	
						45.5	0.012	60.1	0.37		29.0	0.042	39.1	1.13	
31350	−1347.9	0.553	127.0	24.38	1.16	−1346.6	0.417	80.6	3.02	1.39	−1349.9	0.845	100.8	19.43	0.96
	± 5.8	0.019	8.3	1.36		± 4.7	0.026	7.0	0.21		± 4.0	0.047	5.3	0.91	
	−1151.8	0.157	68.8	3.76		−1160.9	0.216	69.1	1.34		−1143.5	0.289	39.7	2.61	
	13.3	0.031	18.6	1.19		8.1	0.026	12.1	0.19		7.3	0.074	11.5	0.56	
31513	−1318.9	0.602	90.1	18.83	1.06	−1304.9	1.081	78.7	7.65	1.06	−1304.1	2.166	79.4	39.24	0.92
	2.7	0.023	4.0	0.68		1.7	0.038	2.4	0.20		2.0	0.125	2.6	1.57	
31903	−1321.6	0.416	101.9	14.72	1.13	−1357.8	0.377	60.3	2.04	1.41	−1311.9	1.014	98.3	22.72	1.34
	4.1	0.020	5.8	0.71		8.7	0.032	10.9	0.34		10.2	0.058	10.2	2.59	
						−1244.8	0.566	48.5	2.46		−1222.4	0.377	23.9	2.05	
						4.8	0.043	8.0	0.37		7.5	0.188	21.1	1.90	
						−1145.0	0.436	20.2	0.79		−1132.6	0.755	16.8	2.90	
						3.4	0.112	6.4	0.12		3.5	0.328	7.7	0.60	
32676	−1290.8	0.383	180.3	23.95	1.44	−1306.6	0.470	100.7	4.25	1.76	−1302.9	1.036	92.4	21.82	1.08
	5.9	0.015	8.5	0.96		3.7	0.023	5.1	0.19		3.4	0.061	4.5	1.02	
	−654.4	0.487	96.4	16.26		−657.1	0.331	106.7	3.16		−747.9	0.262	197.1	11.73	
	3.5	0.022	5.1	0.72		5.2	0.021	7.3	0.18		35.0	0.066	27.2	2.43	
											−652.9	1.268	52.0	15.01	
											3.9	0.151	6.4	2.09	
32923	−1270.5	0.122	136.5	5.79	1.21						−1265.8	0.292	97.6	6.51	0.88
	15.7	0.018	22.6	0.81							8.5	0.034	11.8	0.68	
35079	−1269.4	0.800	132.9	36.94	4.53	−1286.3	1.444	63.8	8.27	1.44	−1280.3	3.141	67.9	48.65	1.66
	2.5	0.020	3.6	0.86		1.3	0.051	1.8	0.21		1.7	0.206	2.1	2.28	
35587											−933.7	0.129	218.8	6.42	0.98
											36.0	0.025	39.7	0.98	